Time-domain analysis of a dynamically tuned signal recycled interferometer for the detection of chirp gravitational waves from coalescing compact binaries

D. A. Simakov
*Institute for gravitational physics, University of Hanover, Hanover, 30167, Germany.**
(Dated: November 21, 2013)

In this article we study a particular method of detection of chirp signals from coalescing compact binary stars – the so-called dynamical tuning, i.e. amplification of the signal via tracking of its instantaneous frequency by the tuning of the signal-recycled detector. A time-domain consideration developed for signal-recycled interferometers, in particular GEO 600, describes the signal and noise evolution in the non-stationary detector. Its non-stationarity is caused by motion of the signal recycling mirror, whose position defines the tuning of the detector. We prove that the shot noise from the dark port and optical losses remains white. The analysis of the transient effects shows that during the perfect tracking of the chirp frequency only transients from amplitude changes arise. The signal-to-noise-ratio gain, calculated in this paper, is ~ 16 for a shot-noise limited detector and ~ 4 for a detector with thermal noise.

I. INTODUCTION

For the last decades a big effort has been made to detect gravitational waves (GWs) from various sources in deep space. In particular, we expect a very interesting kind of GW signal, usually referred to as a chirp signal, to be emitted by compact binary systems, such as a pair of neutron stars or black holes inspiraling towards each other and then coalescing.

The chirp signal gives us unique information about non-linear dynamics of matter and space-time, as the GWs are emitted from the regions with strong space-time curvature. Compact binary coalescence (CBC) and the corresponding GW signal are conventionally split into three stages: inspiral, merger and ring down. The Post-Newtonian approximation of General Relativity (GR) [1–4] allows a precise prediction of most of the inspiral stage. At this stage the signal has a sinusoidal shape with frequency and amplitude increasing in time. The latter stages of the inspiral, and all of the merger and the ring down stages are modeled by Numerical Relativity, and then all stages are continuously sewed together.

Once a signal is measured and compared to the templates, one can extract information about masses and spins of the inspiraling binary objects, as well as the equation of state of dense nuclear matter in the case of the merging neutron stars [5, 6]. Therefore a sensitive detection of chirp signals might verify or falsify GR or alternative theories of gravity via comparing their predictions with the measured parameters. Schutz in [7, 8] also proposed that the Hubble constant can be independently determined in a new and potentially accurate way by observation of the inspiral stage of the chirp GWs.

Nowadays large-scale ground-based laser interferometers make the most sensitive detectors of GWs [9]. Currently the first generation of GW detectors has finished their operation without any detection, which agrees with the estimations for their detection rate. The significantly improved sensitivity of the second generation detector will allow to achieve a detection rate of about 25-400 yr^{-1} [10]. The GW upon reaching the Earth are only tiny perturbations of space-time metric causing small variation of the proper distances between the quasi-free-falling test masses of the laser interferometer. All currently operating and future planned GW detectors are based on the traditional Michelson topology (see FIG. 1): the interferometer consists of a balanced 50/50 beamsplitter, perfectly reflecting end-mirrors and additional mirrors for signal and power amplification, referred to as signal recycling mirror (SRM) and power recycling mirror (PRM), respectively. Interferometers usually operate near the dark fringe in the output port, meaning that the laser beams reflected from the end-mirrors destructively interfere on the beamsplitter towards the photo diode. The

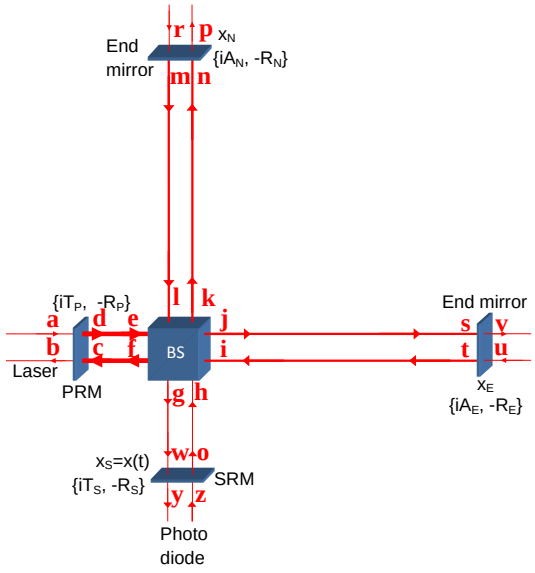

FIG. 1. Scheme of the considered GW detector

* dmitry.simakov@aei.mpg.de

GW causes antisymmetric (differential) motion of the interferometer's end-mirrors relative to the beamsplitter. This breaks the destructive interference at the output port allowing a tiny part of the optical field carrying the information about the GW signal to reach the photodetector. This signal field gets recirculated by the SRM, forming the differential mode of the interferometer in the effective signal recycling cavity (SRC). The PRM in the laser port creates the common mode of the interferometer in the power recycling cavity (PRC) by recirculating the mean laser power reflected from the end-mirrors performing symmetric (common) motion. Therefore the common mode does not contain any information about the GW signal and in the rest of this paper we only consider the differential mode.

Parameters of the SRC are determined by the properties of the SRM: the frequency bandwidth of the cavity is defined by the SRM transmittance and the detuning of laser carrier frequency from cavity resonance is defined by the microscopic position of the SRM. In this sense the SRC is equivalent to a simple Fabry-Perot cavity [11]. The SRC can be tuned to any desired signal frequency via proper choice of the cavity detuning. Currently all GW detectors operate stationary in time, meaning that the parameters of the SRC are fixed. There are two typical regimes of detection of chirp signals in this case: a wide-band operation and a narrow-band operation (see FIG. 2). In the former regime the detector is sensitive to the entire frequency band of the chirp signal, but at moderate sensitivity. On the contrary, in the narrow-band regime the detector is much more sensitive, but only in the narrow band around the signal frequency the SRC is tuned to (see FIG. 2). Since the chirp signal at the inspiral stage is a sine function with frequency increasing in time the peak sensitivity of the narrow-band-operated detector will only be achieved during the short interval of time, when the particular instantaneous frequency of the chirp approximately coincides with the detuning of the SRC.

Another option for the detection of a chirp signal was proposed by Krolak and Meers in [12]: real-time tuning of the SRC to the instantaneous frequency of the signal via positioning of the SRM, i.e. real-time signal tracking. This method of detection is referred to as *dynamical tuning*. However analysis in [12] was performed under the following approximations: (i) a shot-noise limited detector, and (ii) slow enough motion of the SRM such that the detector can be considered as a quasi-stationary one, i.e. all the optical fields evolve adiabatically on the timescale of the motion of the SRM. The latter approximation also sets the limiting instant of time until which the signal can be observed before entering the regime of rapid frequency increase, where quasi-stationary approximation doesn't hold. To agree with these approximations, the authors considered only the detection of part of the chirp signal – with the instantaneous frequency varying from 100 up to 500 Hz. The method we develop in this paper allows us to treat the problem of dynamical tuning

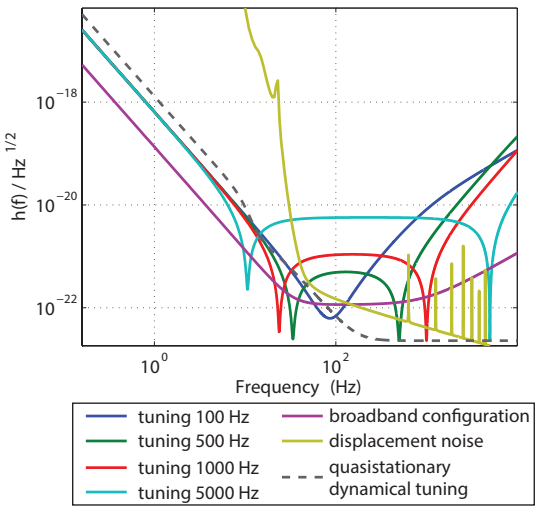

FIG. 2. The quantum noise of broadband and narrowband detector configurations. The quantum noise of a quasistationary dynamical tuning (The points of optical resonance in curves corresponding to each tuning) is also presented with respect to mirror displacement noise

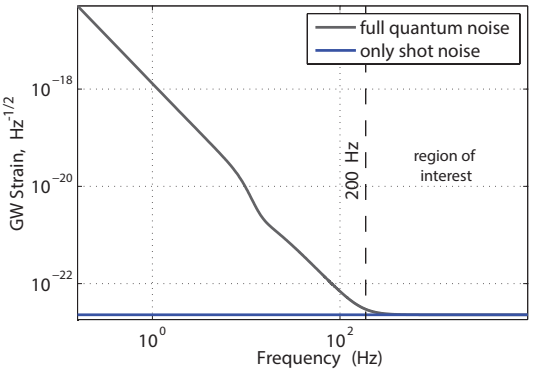

FIG. 3. The quasistationary appoximations for the full quantum noise (with radiation pressure) and for the shot noise only of dynamical tuning

outside of these approximations. It should be noted that we do not consider the problem of signal prediction; we only assume that the initial time evolution of the signal is known, for instance, from the low-frequency data of other GW detectors, such that subsequent evolution of the signal can be predicted.

The response of a stationary-operated detector to GWs and all kinds of noise sources is usually calculated in the frequency domain. For the detailed analysis see references [9, 13–17]. However, a GW detector performing dynamical tuning operates in the non-stationary regime, where frequency domain analysis is not adequate and therefore we perform a time-domain consideration. In particular, the detector response takes the form of a series over an infinite number of round trips of light inside the SRC [18, 19], the so-called impulse response. Some

aspects of both time-domain and frequency-domain analyses of laser GW detectors are given with sufficient details, including the responses to common and differential modes of a stationarily operating interferometer, and its shot-noise sensitivity formulas, in [20]. Using time-domain model we calculate the response of the detector to the shot noise (vacuum fluctuation of the electromagnetic field injected from the dark port or lossy optical elements) and to differential motion of the end-mirrors (caused by the GWs and various noise forces such as thermal noise). The radiation pressure noise (back action) is omitted in the current model because (i) its typical frequencies are lower than characteristic frequencies of the considered part of chirp signals starting from 200 Hz (see FIG. 3), (ii) it is dominated by the other noise sources (see FIG. 2). Finally we compute the increase of the signal-to-noise ratio (SNR) as compared to the SNR of the traditional broad-band stationary operated detector. For the shot noise limited detector the increase of SNR is ~ 16, for the detector with thermal noise the increase is ~ 4. Therefore we found that in contrast to the stationary operated detector limited by both thermal and shot noise, the detector performing dynamical tuning is only thermal noise limited. This happens because thermal noise and GW signal, both creating the differential motion of the end-mirrors, are resonantly enhanced by dynamical tuning in the same manner (effectively, dynamical tuning tracks and amplifies the same components of thermal noise as of the GW signal), while shot noise on the photo detector remains the same (more precisely, shot noise remains delta-correlated independently of the motion of the SRM).

The paper is organized as follows. We derive the time-domain response of the detector to a gravitational wave and to thermal noise in section II and to the shot noise in section III. In section IV we present the SNR gain with respect to a stationary detector which can be achieved with dynamical tuning.

II. DETECTOR RESPONSE ON A DIFFERENTIAL END-MIRROR MOTION

Denote the differential motion of the end-mirrors as

$$x_{\rm D}(t) = \frac{x_{\rm E}(t) - x_{\rm N}(t)}{2}, \qquad (1)$$

where $x_E(t)$ and $x_N(t)$ are the displacement of the east and the north end-mirrors, respectively (see FIG. 1). The connection between the differential motion of the end-mirrors and the GW strain $h(t)$ is the following in the case of zero initial coordinate and velocity:

$$x_{\rm D}(t) = \frac{Lh(t)}{2}, \qquad (2)$$

where L is the arm length.

The output current on the photodetector $z(t)$ contains the information about the differential motion of the end-mirrors, caused by gravitational waves, and delivered by

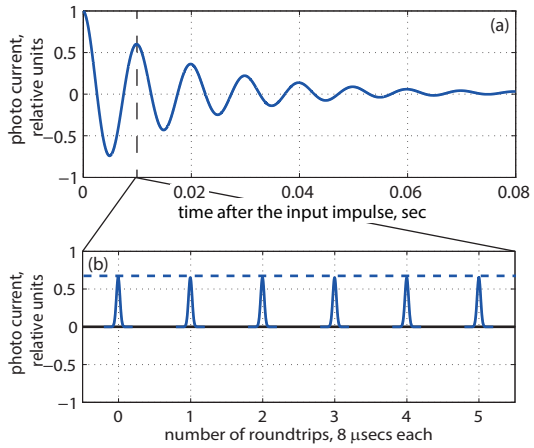

FIG. 4. The typical impulse response of the considered detector with a constant detuning $f_{\rm tun} = 100$ Hz: (a) in the response decay-time scale, (b) in the single round-trip time scale

the subsequent circulation of the laser field inside the SRC. The response of the detector to the signal can be considered as linear, since the end-mirror displacements are small in comparison to the wavelength of the laser, and since the fields inside the cavity are subject to the superposition principle. In the time domain the impulse response of the detector is described with a so called impulse response $L_{S\to C}(t, t_1)$ determined as:

$$I_{\rm y}(t) = \int_{-\infty}^{t} L_{\rm S\to C}(t, t_1) x_{\rm D}(t_1) dt_1, \qquad (3)$$

here $S \to C$ stands for "signal to current", $I_{\rm y}(t)$ is the photocurrent after the detection of the field y.

The physical meaning of the impulse response is the output response of the detector to a delta-impulse shaped signal in the instance of time t_1 in the input. Hence it contains the information about the signal transformation in the detector, and the physics related to it. The change in time of the SRM position makes detector non-stationary, the description of which requires the impulse response as a function of two independent time-variables.

The impulse response of the detector to the differential mirror motion, derived in appendix B, explicitly reads:

$$L_{\rm S\to C}(t, t_1) = \sum_{n=0}^{\infty} C_n \cos(\xi_n(t)) \times \\ \times \delta\left(t_1 - t + n\tau + \frac{\tau}{2}\right), \qquad (4)$$

where

$$C_0 = -4\sqrt{2}\sqrt{\frac{\pi\hbar\omega_p}{\mathcal{A}c}}R_{\rm F}T_{\rm S}|E|k_{\rm p}, \tag{5a}$$

$$C_n = C_0(R_F R_S)^n, \tag{5b}$$

$$\xi_0(t) = \phi_{\rm h}, \tag{5c}$$

$$\xi_n(t) = \phi_{\rm h} + 2k_{\rm p}\sum_{k=1}^{n} x(t-k\tau). \tag{5d}$$

For the notations and definitions of this equation see Table I

The plot of the impulse impulse depicted in FIG. 4. For all the simulations in this paper we use the parameters from tables II, III.

The delta-like impulse in the differential motion of the end-mirrors modulates the phase of the laser fields at their surfaces. These fields are formed from the field E falling on the beamsplitter. Time scales of phase modulations should be longer than 1 optical cycle $t_{\rm di} \gg 1/\omega_{\rm p}$. The phases of the modulations in the arms have the opposite signs, therefore they interfere constructively towards the dark port on the beamsplitter forming the amplitude modulation, which has the shape of a short laser impulse. The interference is reversible, hence it is convenient to consider the evolution of the perturbations, caused by differential end-mirrors motion, as the propagation of the amplitude modulation inside the single equivalent Fabry-Perot cavity formed by the SRM and the end-mirror with the reflectivity

$$R_{\rm F} = \frac{R_{\rm E} + R_{\rm N}}{2}. \tag{6}$$

The time the light requires for the round trip inside the equivalent cavity is

$$\tau = 2\frac{L}{c}, \tag{7}$$

where L is the length of the light path from the SRM to the end-mirrors and, subsequently, the length of the equivalent cavity. The smaller part of the laser impulse that reaches the SRM is transmitted with the coefficient T_S, while the rest of it is reflected with, respectively, R_S. The reflected part comes back to the SRM after the full roundtrip and the process repeats infinitely. As the result we have an infinite number of decaying "echo"-impulses with corresponding amplitudes $C_0, C_1, C_2, ...$ on the photodiode. The decay factor during one round trip is $R_{\rm S}R_{\rm F}$, and the phase shift between two consequent impulses, k-th and (k+1)-th, reads

$$\delta(t'_k) = 2k_{\rm p}x(t'_k), \tag{8}$$

where $t'_k = t_1 + k\tau + \tau/2$ is the reflection instance of the k-th impulse, and x(t) is the microscopic displacement of the SRM from the resonant position of the equivalent cavity. The output light is converted to the directly

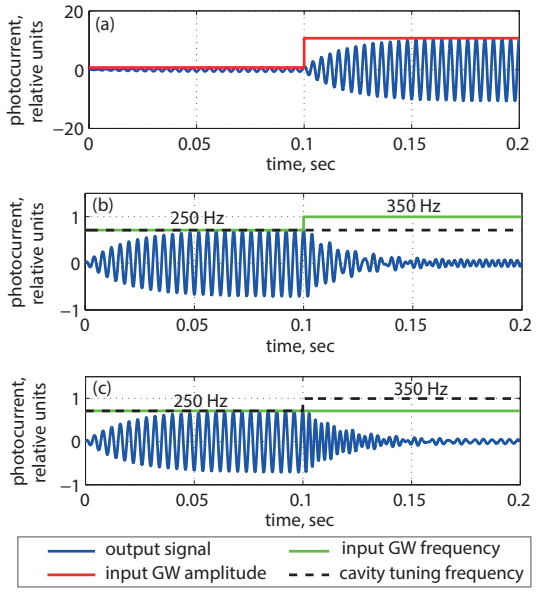

FIG. 5. The typical transients of the considered detector on the step-wise change of (a) $X(t)$, (b) $f(t)$, (c) $\delta(t)$

measured current via homodyne detection with the local oscillator (LO) field

$$y_{\rm LO} = \sin(\omega_{\rm p}t + \phi_{\rm LO}), \tag{9}$$

where ϕ_{LO} is a phase of the LO. The latter together with the phase of field incident on the beamsplitter E determines the homodyne angle

$$\phi_{\rm h} = \phi_{\rm LO} + \phi_{\rm E}, \tag{10}$$

specifying the quadrature of the modulation we detect.

On the plot of the impulse impulse, depicted in FIG. 4, its typical dynamical transient features become apparent. The decaying oscillations of the envelope, being the beating between detector sideband and local oscillator, represent respectively the detuning, which can be also time-dependent, and the relaxation time of the SRC, while the delays between impulses show the roundtrip time.

The detailed mathematical derivation of (4-5) and the explanation of the time-domain model for the GEO 600 optical layout is described in appendix B. The simple case of a Fabry-Perot cavity is treated in appendix A.

Because of its sinusoidal shape the differential mirror motion caused by chirp GWs are described in the following form:

$$x_{\rm D}(t) = X(t)\cos\zeta(t), \tag{11}$$

where $X(t)$ and $\zeta(t)$ are the time-dependent amplitude and phase correspondingly. The latter is related to the frequency of the signal: $\zeta(t) = \int_{t_0}^{t}\Omega(t_1)dt_1$, where $\Omega(t) = 2\pi f(t)$ is an angular frequency.

TABLE I. Notations and definitions used in this paper.

Notation	Definition
ω_p	the frequency of the carrier laser
c	the speed of light
$\mathcal{A}$	the cross-section of the detected beam
$R_{\rm F}$	the equivalent end-mirror reflectivity (6)
$T_{\rm S}$	the transmittance of the SRM
$R_{\rm S}$	the reflectivity of the SRM
E	the field falling on the beamsplitter (see FIG. 1)
$k_{\rm p}$	the wave vector $\frac{\omega_{\rm p}}{c}$
ϕ_h	the homodyne angle (10)
$x(t)$	the microscopic displacement of the SRM from the resonant position
τ	the round-trip time (7)

Cavity is resonant to only one of the sidebands, while the other one is suppressed. The tuning of the sideband takes place, when the additional phase shift of the laser field during one round-trip, caused by the GW oscillations, is canceled by the corresponding displacement of the SRM from the laser resonance position. Generally speaking, this condition is defined within one roundtrip and therefore we can express it mathematically for the non-stationary detector with the moving SRM:

$$\delta(t) = \zeta(t+\tau/2) - \zeta(t-\tau/2) \approx 2\pi f(t)\tau. \qquad (12)$$

The dynamical tuning detection, following this resonant condition is referred to as *resonant tracking* of the signal. The similar task of *dynamic resonance* of the Fabry-Perot cavity to the perturbations of the laser phase inside it is considered in details in [21].

The impulse response allows studying the dynamical behavior of the laser field perturbations inside the SRC via transient effects, i.e. the response of the detector to the step-wise change of the parameters, namely the signal amplitude $X(t)$, the signal frequency $f(t)$, and the detuning of the SRC $\delta(t)$, to their new values. For convenience, all the considered examples start from the resonant case. The three transients depicted in FIG. 5 display the relaxation processes of the same duration as the impulse response (FIG. 4). Each of the transients caused by changes of frequency: either of the GW signal in FIG. 5(b) or of the SRC detuning in FIG. 5(c), contains clearly distinguishable processes at the new frequencies. All the fields, stored in the cavity before the step-change, decays and oscillates at the frequency of the after-step SRC detuning, instantaneously changed to it if applicable. At the same time, the detector accumulates the new field on the GW frequency corresponding to the new stationary parameters of the GW signal and detector.

The remarkable consequence of the described processes becomes apparent as we perform the resonant tracking (12) to the step-change of GW frequency, i.e. when both frequencies of the GW and of the SRC detuning are changing synchronized, depicted in the FIG. 6(a). The perturbations caused by these changes are canceled, so the frequency of the output signal switches instantaneously form one value to another without any relaxation processes. Hence, only amplitude transient effects affect the output signal during the resonant tracking of the GW with both frequency and amplitude dependent on time.

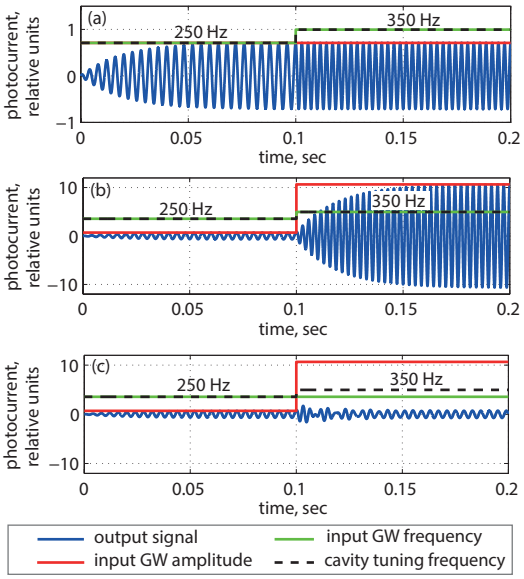

FIG. 6. The transients of the considered detector on the combinations of step-wise changes of (a) $f(t)$ and $\delta(t)$, (b) $X(t)$, $f(t)$ and $\delta(t)$, (c)$X(t)$ and $\delta(t)$

A more general analytical calculation of the output signal (3 - 5) from the resonant tracking (12) of the sinusoidal GW signal (11) brings us to the same conclusion. The explicit expression can be obtained by expansion of cosines into complex exponents and leaving only the resonant sideband terms, assuming the non-resonant fields, being summed up with random phases, to be insignificant. The consideration of the time-dependent amplitude in the frequency domain and subsequent reducing of the derived geometric series brings us to the following result:

$$y_{\rm PD}(t) = Y(t)\cos\zeta(t-\tau/2), \qquad (13)$$

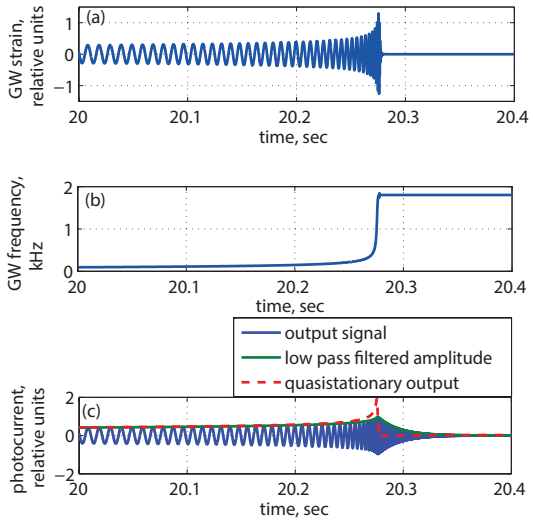

FIG. 7. (a) The gravitational wave signal from the 5+5 Solar mass spinless black hole binary. (b) The instantaneous frequency of this signal. (c) The resonantly tracked detection signal, compared to the low-pass-filtered GW amplitude and the output in quasistationary approximation

where the Fourier transform of $Y(t)$ reads:

$$Y(\Omega) = R(\Omega)X(\Omega), \tag{14}$$

and

$$R(\Omega) = \frac{1}{2}\frac{C_0 e^{i\Omega\tau/2}}{1 - R_S R_F e^{i\Omega\tau}}. \tag{15}$$

The transfer function here is an Airy function for the equivalent Fabry-Perot cavity with the frequency bandwidth calculated from

$$\gamma = \frac{T_S^2 + T_F^2}{2\tau}, \tag{16}$$

and equal to 8.3 Hz. Here $T_F^2 = 1 - R_F^2$ is a transmittance (or losses) of the end-mirror of an equivalent FP cavity.

The phase and the frequency behavior of the output signal here mirrors that of the input GW, while the amplitude at the output is smoothed with respect to the amplitude of the GW signal. In other words, during the resonant tracking the shape of the output signal is obtained by low pass filtering of the GW signal.

The simulated resonantly tracked detection of the chirp signal (3 - 5) compared to the independently low-pass-filtered GW amplitude (FIG. 7(c)) confirms the amplitude-only nature of perturbations of the GW signal inside the detector. We can see that influence of the non-resonant sideband is negligible here.

The inverse impulse response, obtained from (4) and (5) allows to deconvolute the gravitational wave shape from the signal on the photo diode and the known motion law of the SRM:

$$L_{C\to S}(t, t_1) = \sum_{n=0}^{\infty} \tilde{A}_n(t)\delta(t_1 - t - \tau/2 + n\tau), \tag{17}$$

where:

$$\tilde{A}_0(t) = \frac{1}{C_0}, \tag{18a}$$

$$\tilde{A}_1(t) = -\frac{R}{C_0}\cos\left(2k_p x(t - \tau + \tau/2)\right) \tag{18b}$$

$$\tilde{A}_2(t) = \frac{R^2}{C_0}\sin\left(2k_p x(t - \tau + \tau/2)\right) \times \times \sin\left(2k_p x(t - 2\tau + \tau/2)\right) \tag{18c}$$

$$\tilde{A}_n(t) = \frac{R^n}{C_0}\prod_{l=2}^{n-1}\cos\left(2k_p x(t - l\tau + \tau/2)\right) \times \times \sin\left(2k_p x(t - \tau + \tau/2)\right) \times \times \sin\left(2k_p x(t - n\tau)\right), n \geq 3. \tag{18d}$$

The following equation proves that the eigenbases of both direct and inverse impulse response transformations are full, and theoretically no information about the GW signal is lost during the resonant tracking:

$$\int_{-\infty}^{\infty} L_{C\to S}(t, t_1) L_{S\to C}(t_1, t_1') = \delta(t - t_1'). \tag{19}$$

The influence of the differential end-mirror motion caused by thermal noise [22, 23] can also be calculated, using (4):

$$B_{th}(t_1, t_2) = \sum_{m=0}^{\infty}\sum_{n=0}^{\infty} C_m C_n \cos\xi_m(t_1)\cos\xi_n(t_2) \times \times B(t_2 - t_1 + (m - n)\tau), \tag{20}$$

where $B(\tau)$ is the stationary autocorrelation function of the thermal differential end-mirror motion, corresponding to the known spectral density $S(\Omega)$ (see e.g. FIG. 10).

III. DETECTOR RESPONSE TO THE SHOT NOISE

Quantum shot noise is conventionally considered as ground state quantum oscillations injected into a cavity from the dark port and from lossy elements [13]. Since Maxwell's equation is valid for quantum mechanics, the quantum operator of the electromagnetic field can be treated like the classical field values in the previous section.

The quantum electrical field operator reads:

$$\hat{E}_A(t) = \int_0^{\infty} \sqrt{\frac{2\pi\hbar\omega}{\mathcal{A}c}}[\hat{a}(\omega)e^{-i\omega t} + \hat{a}^+(\omega)e^{i\omega t}]\frac{d\omega}{2\pi} \approx \approx \sqrt{\frac{2\pi\hbar\omega_p}{\mathcal{A}c}}[\hat{a}(t)e^{-i\omega_p t} + \hat{a}^+(t)e^{i\omega_p t}], \tag{21}$$

where $\hat{a}(\omega)$ and $\hat{a}^{+}(\omega)$ are the annihilation and creation operator in the point a in FIG. 1 (the electromagnetic operators in the other locations are denoted by the corresponding letter), and $\mathcal{A}$ is the effective optical cross section of the considered beam.

The ground state oscillation (21) detected with the local oscillator (9) gives white noise in the frequency band of detection:

$$B_{\rm in}(t_1,t_1) = C_z\delta(t_1-t_2), \tag{22}$$

where

$$C_z = \frac{\pi\hbar\omega_{\rm p}}{2\mathcal{A}c}. \tag{23}$$

The linear transformations of the vacuum fluctuations inside the detector, namely phase shift, propagation and the amplitude change, are described by the complex impulse response of the field amplitude operator:

$$\hat{\rm y}(t) = \int_{-\infty}^{t} L^{\rm c}(t,t')\hat{\rm z}(t')dt', \tag{24}$$

where $L^c(t,t_1)$ is a complex impulse function, $\hat{y}(t)$ and $\hat{z}(t)$ are the amplitudes of the output and input respectively (see FIG. 1).

The statistical averaging of the current after the homodyne detection (9) of the output vacuum fluctuation, keeping in mind (22), reads:

$$B_{\rm vac}(t_1,t_2) = C_{\rm z}\int_{-\infty}^{\min(t_1,t_2)} dt_1'\times \\ \times\,\Re\left(L_{\rm S}(t_1,t_1')L_{\rm S}^{*}(t_2,t_1')\right). \tag{25}$$

Here:

$$L_{\rm S}(t,t_1) = L^{\rm c}(t,t')e^{i\omega_p(t-t_1)} \tag{26}$$

is an impulse response of the output field amplitude $\hat{y}(t)$ to the input one $\hat{z}(t)$ in the rotating frame, i.e. excluding the time evolution of the phase. Explicitly the function is:

$$L_{\rm S}(t,t_1) = \sum_{n=1}^{\infty} T_{\rm S}^2\exp\left[i\varphi_n(t)\right]R_F^n R_S^{n-1}\delta(t_1-t+n\tau) - \\ - R_{\rm S}\delta(t_1-t)\exp i\varphi_0(t), \tag{27}$$

where

$$\varphi_0(t) = -2k_{\rm p}x(t), \tag{28a}$$

$$\varphi_1(t) = 0, \tag{28b}$$

and

$$\varphi_n(t) = 2k_{\rm p}\sum_{k=1}^{n-1}x(t-k\tau). \tag{28c}$$

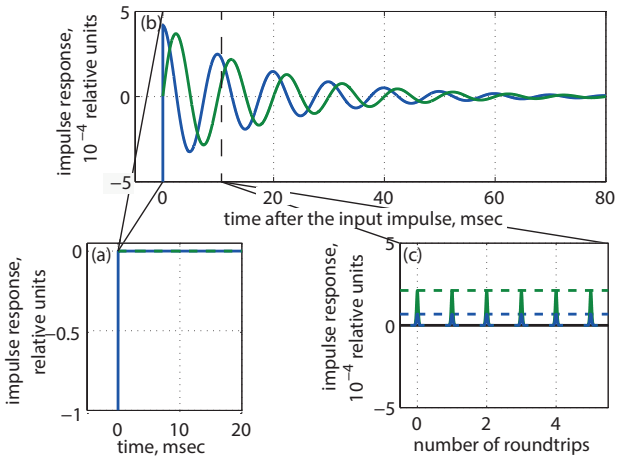

FIG. 8. Two quadratures of the impulse response to the vacuum quantum oscillations, injected from the dark port: (a) on the large amplitude scale, depicting the direct reflection of the impulse from the SRM inpulse, (b) on the small amplitude scale, representing SRM transmission from the inner SRC oscillations and decay, (c) on the short time scale, picturing the discrete nature of the impulse function and the round-trip time

A more detailed derivation of the response impulse is presented in appendix B.

The plot of the impulse response is presented in FIG. 8. The delta-like impulse, sent to the dark port $\hat{z}(t)$, is reflected back from the SRM almost completely ($R_{\rm S}\approx 1$), only a tiny fraction of it is injected into the detector and does the roundtrips the way it was mentioned in the previous section.

For convenience of transformations and simplification of the expressions, one can introduce a new value Φ_i such, that

$$\Phi_1 \equiv 0, \tag{29a}$$

$$\Phi_N \equiv \sum_{k=1}^{N-1} 2k_{\rm p}x(t_0+k\tau), N>1, \tag{29b}$$

$$\varphi_n(t) = \Phi_N - \Phi_{N-n+1}, \forall n \geq 0, \tag{29c}$$

where t_0 is an appropriate moment of time close to the beginning of the detection. The physical meaning of Φ_i is a phase that the imaginary laser field, injected into the cavity at t_0, would get after $i=(t-t_0)/\tau$ roundtrips inside the cavity. The reflection from the SRM during each roundtrip would introduce an individual phase shift corresponding to the microscopic position of the SRM. Except for a constant, it equals the phase of the GW sinusoidal signal, $\zeta(t)$, to which this SRM motion is resonant (12).

After substitution of (27) into (25) and some simplifi-

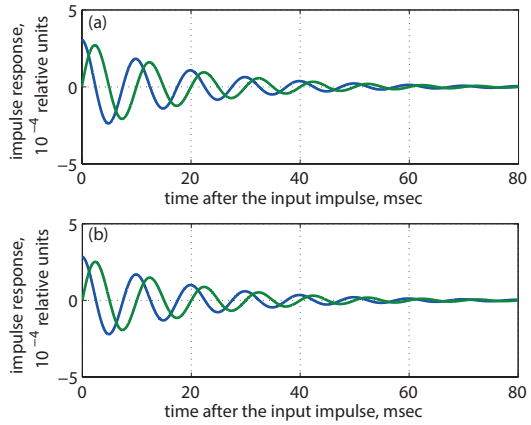

FIG. 9. Two quadratures of the impulse response to the vacuum quantum oscillations, injected from the equivalent end-mirrors: (a) from the north end-mirror, (c) from the east end-mirror

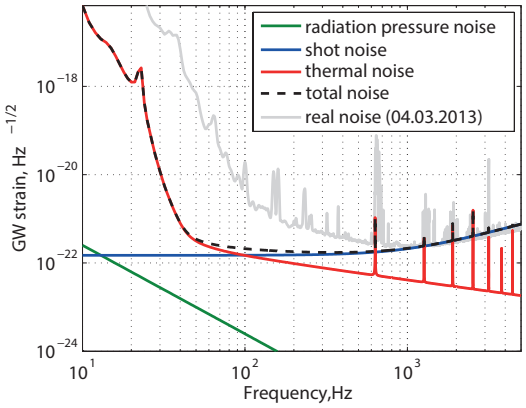

FIG. 10. The noise budget of GEO 600. The gain of the real noise at high frequencies is due to the injection of squeezed light

cations we get:

$$B_\eta(t_1,t_2) = C_\mathrm{z}\sum_{n=-\infty}^{\infty}\cos(\Phi_N-\Phi_{N-n})R_\mathrm{F}^{|n|}T_\mathrm{S}^2R_\mathrm{S}^{|n|}\times$$
$$\times\left[\frac{-1+R_\mathrm{F}^2}{1-R_\mathrm{F}^2R_\mathrm{S}^2}\right]\delta(t_1-t_2-n\tau)+C_\mathrm{z}\delta(t_1-t_2). \quad (30)$$

The autocorrelation function for the detector with ideally reflecting end mirrors $R_\mathrm{F}=1$ keeps only one non-zero summand $C_\mathrm{z}\delta(t_1-t_2)$, meaning the detected shot noise is white. Despite the non-trivial transformation of the electromagnetic field of the quantum oscillations inside the detector (27), its statistics remain the same.

The optical losses of the ground mode of the laser field inside a cavity, caused by the scattering into higher order modes, reflection from the AR coating of the beam splitter and the absorptions in all optical elements, decreases the effective reflectivity of the equivalent mirror $R_\mathrm{F}<1$, and therefore modifies the statistics of the corresponding output noise in (30). However, the losses cause additional noise due to the fluctuation-dissipation theorem [24], which can be equivalently considered as the injections of the ground state vacuum quantum oscillations through the equivalent mirrors [13] with a transmittance equal to the optical losses in the arms (A_E and A_N in FIG. 1). The corresponding impulse responses read in a similar manner to (27):

$$L_{\mathrm{S,N}\to\mathrm{C}}(t,t_1) = A_\mathrm{N}T_\mathrm{S}\frac{\sqrt{2}}{2}\sum_{n=0}^{\infty}(R_\mathrm{F}R_\mathrm{S})^n\times$$
$$\times\exp[i(\Phi_N-\Phi_{N-n})]\delta\left(t_1-t+\frac{\tau}{2}+n\tau\right). \quad (31a)$$

$$L_{\mathrm{S,E}\to\mathrm{C}}(t,t_1) = A_\mathrm{E}T_\mathrm{S}\frac{\sqrt{2}}{2}\sum_{n=0}^{\infty}(R_\mathrm{F}R_\mathrm{S})^n\times$$
$$\times\exp[i(\Phi_N-\Phi_{N-n})]\delta\left(t_1-t+\frac{\tau}{2}+n\tau\right). \quad (31b)$$

Their plots are depicted in FIG. 9.

And therefore, the autocorrelation function of their total noise on the PD is

$$B_{\eta\,\mathrm{F}}(t_1,t_2) =$$
$$= C_\mathrm{z}(R_\mathrm{F}R_\mathrm{S})^{|n|}T_\mathrm{S}^2\sum_{n=-\infty}^{\infty}\cos(\Phi_N-\Phi_{N-n})\times$$
$$\times\frac{1-R_\mathrm{F}^2}{1-[R_\mathrm{F}R_\mathrm{S}]^2}\delta(t_1-t_2-n\tau). \quad (32)$$

The total output shot noise of the non-stationary detector with the moving SRM, including the injections of the ground state oscillation from the dark port (30) and from the optical losses (32) is white:

$$B_\eta^\mathrm{tot}(t_1,t_2) = C_\mathrm{z}\delta(t_1-t_2). \quad (33)$$

IV. BENEFITS OF DYNAMICAL TUNING AND OF THE TIME-DOMAIN MODEL

The main goal of any detector development is increasing the sensitivity. Therefore this property of the dynamical tuning should be tested. The signal-to-noise-ratio (SNR) is a common value, derived from both Wiener filtering [25] and the Neyman-Pearson criteria (See Appendix C), describing the sensitivity of a certain detection regime with an arbitrary, also non-stationary, known Gaussian noise budget to a given signal.

GEO 600 [26, 27] is the only currently operating detector traditionally used for testing advanced technologies, such as signal recycling or squeezing. For simplicity we

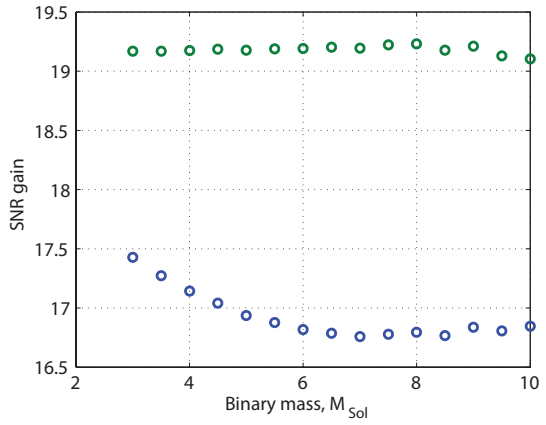

FIG. 11. The SNR gain of the dynamical tuning in comparison with the stationary broadband regime. Both regimes are considered as shot noise limited

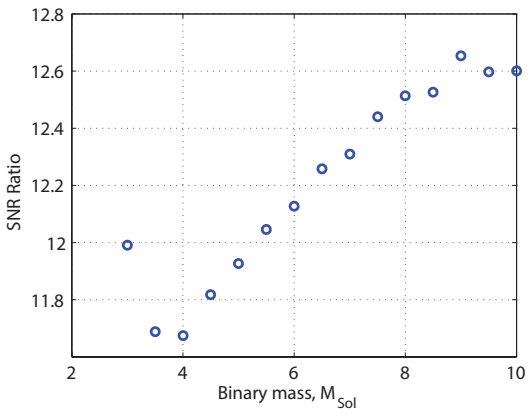

FIG. 12. The ratio of SNRs for a shot noise limited and a thermal noise limited detector with dynamical tuning

replace each folded arm of GEO 600 by a straight arm with the same optical length. The stationary regime of GEO 600 has a broad frequency band ($\sim$ 1000 Hz), established by a low-reflective SRM, and is therefore optimized for chirp signals. The dynamical tuning can be implemented into GEO 600 by: (i) installation of a new SRM with high reflectivity, instead of the old one, to achieve the narrow-band regime, and (ii) moving the SRM very precisely, synchronized to the chirp frequency change, also keeping the detector locked. The considered parameters of GEO 600 in both regimes are presented in the TABLES II and III.

The chirp signals are modeled by using hybrid models [1–4] for an arbitrary set of masses and spins of the binary elements. For convenience only one group of signals is analyzed: spinless binaries with equal masses and total mass ranging from 3 to 10 solar masses. The significant benefits from the dynamical tuning arise at the very last stages of the chirp, with high rate of change of frequency. Therefore, we consider for each signal only the part starting from 100 Hz of the instantaneous frequency, as it shown for example in FIG. 7. The signal part of the photocurrent from the chirp is simulated according to the algorithm described in appendix D, based on the equations (4, 5).

The noise of the detector can be divided into three parts, according to their origins: shot noise, radiation pressure noise and thermal noise as it is shown in FIG. 10 [22, 23]. We assume, that the real noise will be reduced to the theoretical predictions, and we use them for the analysis. The radiation pressure noise is negligible in the frequency band of our interest. The increase in sensitivity occurs from the enhancement of the GW signal in comparison to shot noise only, because dynamical tuning amplifies the same components of thermal noise as of GWs (20). Therefore we first compare two regimes in the shot noise limited assumption. Though currently the shot noise in GEO 600 is squeezed, for the sake of clarity we consider in this paper the ground state shot noise as a model for the reference regime. We do not also need the squeezing during the dynamical tuning, because the shot noise is low enough to overcome the thermal noises, as it will be shown later.

The ground state shot noise on the photodiode remains delta-correlated independently from the changed parameters of the SRM, namely its motion during the detection and its transmittance (see Sec. III). Therefore the SNR in both regimes, the broadband and the dynamical tuning, can be calculated with the following formula, derived in appendix C, by substituting the corresponding simulated signal parts of the photocurrent (C10):

$$d^2 = \frac{1}{C_z}\int_0^T s^2(t)dt. \tag{34}$$

The gain in the SNR for the shot-noise limited detector, presented in FIG. 11, decreases with increasing mass of the system. The difference between dynamical tuning and quasi-stationary approximation is presented in FIG. 7, but due to slow change of frequency and amplitude for most of signal duration the integral effect is of the order 15 %.

The thermal noise in FIG. 10 is comparable to the shot noise in the frequency band of interest. Since dynamical tuning decreases dramatically the influence of shot noise to the sensitivity, the influence of the thermal noise, which stays the same, the latter becomes dominating, as it shown in FIG. 12. Therefore the thermal noise limited detector makes a good approximation for the SNR gain achievable by dynamical tuning in a real detector with both shot and thermal noise, as is depicted in FIG. 13.

V. DISCUSSION

The set of SNRs for the dynamical tuning we presented in the previous section was obtained with very special as-

TABLE II. Unchanged GEO 600 parameters.

Symbol	Quantity	Current configuration value
A_{E}^2	Equivalent power transmission on the east mirror (losses at the mirrors + scattering on the beam splitter (BS))	450 ppm (10^{-6})
A_{N}^2	Equivalent power transmission on the east mirror (losses at the mirrors)	390 ppm
L	Effective length of the arm	1200 m
W_{E}	Power on the beam splitter (E in FIG.1)	2.12 kW

TABLE III. GEO parameters, modified for the dynamical tuning.

Symbol	Quantity	Current configuration value	Value for dynamical tuning configuration
T_{S}^2	Power transmission on the signal recycling mirror (SRM)	0.1	420 ppm
δ	Frequency detuning of signal recycling cavity	0 Hz	resonant tracking

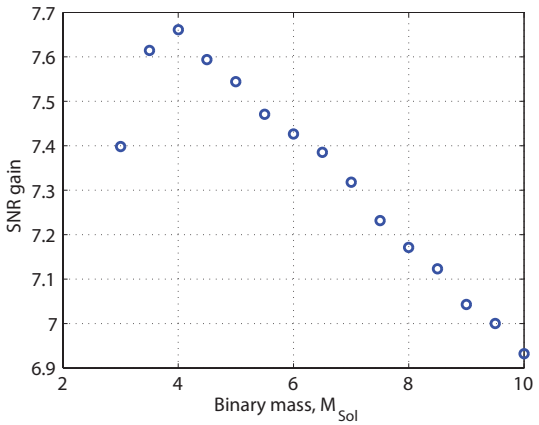

FIG. 13. The SNR gain of the dynamical tuning compared to broad band configuration, assuming that dynamical tuning is thermal noise limited

sumptions: (i) the SRM tracks resonantly the frequency of the chirp signal (12), (ii) the detector is considered to be either thermal, or shot noise limited. The inevitable error in the SRM position during its motion makes perfect resonant tracking of the signal impossible, preventing the signal and thermal noise from reaching their maximal amplification in comparison to shot noise. Even a small error, comparable with the band-width of the dynamically tuned detector, i.e. 8 Hz, makes the influence of shot and thermal noise of the same order.

The calculation of the SNR for both noise terms, using (C7), requires in this case a numerical solving of the integral equation (C5) with the composite detector noise, which can be in principle calculated with an arbitrary precision,

$$B_{\mathrm{tot}}(t_1,t_2) = B_{\eta}^{\mathrm{tot}}(t_1,t_2) + B_{\mathrm{th}}(t_1,t_2), \qquad (35)$$

where the items from the sum are taken from (20) and (33) respectively. The solution of (C5) allows also to estimate the influence from the signal tracking error, as it was done in [12], giving us the realistic benefits of the dynamical tuning.

In all the real GW-detectors, dc-readout is used instead of homodyne detection [28]. The additional leak of laser light from the power recycling cavity, caused by the dark-fringe offset, becomes an equivalent local homodyne oscillator. The leaking power on the photodiode

depends on the SRC detuning, and therefore becomes time-dependent during the dynamical tuning detection. The filtering of the new time-dependent "DC"-part of the photo-current requires new solutions in the signal processing.

The considered Michelson configuration is used only in GEO 600, while the other GW detectors, namely Advanced LIGO, Advanced VIRGO and the Einstein Telescope, have Fabry-Perot cavities in the arms. The time-domain model for their layout may be obtained by the development of the described time-domain model. However, the shot and the thermal noise of these detectors have similar proportions as depicted in FIG. 10, therefore the thermal-noise-limited configurations will give a good approximation for the maximal sensitivity gain which is possible by the implementation of dynamical tuning.

VI. CONCLUSIONS

In this paper we have considered the problem of dynamical tuning – a particular method of detecting a chirp signal, when the GW detector is kept resonantly tuned to the instantaneous frequency of the signal via properly shifting the SRM in time. We have developed a time-domain method of analysis since the detector performing dynamical tuning operates in a non-stationary regime (detuning of the SRC rapidly changes in time to match the frequency of the signal). We have considered the response of the detector to the shot noise injected through the dark port and lossy optical elements, and differential motion of the end-mirrors, in particular, GW signal and thermal noise. We found that although the optical fields describing vacuum fluctuations transform non-trivially inside the non-stationary detector, the output shot noise remains delta-correlated for arbitrary realistic motions of the SRM. For an ideal tracking of the GW signal we calculated the SNR gain of a dynamically tuned detector with only shot noise to be around 16, as compared to the corresponding broadband stationary configuration. For non-ideal tracking one will have to take into account transient processes, but this was out of the scope of the current work, although various transient processes in detector responses were analyzed. However, it is also physically clear that the components of the GW signal and of the thermal noise are resonantly enhanced in the same manner (both represent differential motion of the end-mirrors), therefore the dynamically tuned detector becomes thermal noise limited as compared to a stationary interferometer limited by both thermal and shot noise. We found the SNR gain relative to thermal noise to be around 4, therefore the shot-noise-limited SNR gain can only be achieved when the power of the thermal noise is decreased more than factor of four.

The fast changes of the signal frequency and amplitude as well as of the SRM position cause transient effects. However, by properly adjusting the mirror motion to the signal frequency, the transient effects are canceled by each other.

Assuming a shot noise limited detector the enhancement factor in SNR over the current broadband GEO 600 configuration is 17. The influence of dynamical effects in the chirp signal detection is of the order of 15 percent. However we can neglect them if we perfectly track the signal frequency, because then the detector becomes both thermal noise limited, and without any transient effects of the gravitational wave and displacement noise related to each other. Also the current level of thermal noise reduces the SNR enhancement factor down to 7.

This number is the upper limit for the SNR gain for dynamical tuning with the theoretically predicted thermal noise and we could achieve the value of 17 if we could decrease the thermal noise sufficiently. The enhancement values will also be modified when we take into account the error of the resonant tracking that will cause a contribution of both shot and thermal noise into the dynamical tuning sensitivity.

ACKNOWLEDGMENTS

I want to thank TFB-SR7 and the Max-Planck Society, who paid my salary and stipend, and the Max-Planck Institute and personally Karsten Danzmann for providing me comfortable material conditions for my scientific investigations.

I would like to extend my appreciation to the people who helped me with the scientific part of this work: to Harald Lück for supervising my job, to Sergey Tarabrin for many hours of fruitful discussions, explaining fine points in physics of GW detectors, to Denis Vasilyev for giving a glance to my work from the non-related to GW society point of view, to Valentin Averchenko for the discussion of the mathematical issues, to Parameswaran Ajith and especially Frank Ohme for explaining the behavior of compact binaries, to Andrzej Krolak for discussion of the dynamical tuning idea.

I would like to mention Farid Khalili, Niels Lörch and Katherine Dooley for giving important remarks concerning this text, and especially Holger Wittel and Sergey Tarabrin for putting much efforts into writing it.

Appendix A: The impulse response of a Fabry-Perot cavity

A Fabry-Perot cavity (FIG. 14) makes the simplest model for a dynamically tuned gravitational wave detector, more particularly for the SRC [11] .

Plane electromagnetic waves make a good approximation for the light inside the Fabry-Perot cavity:

$$\hat{E}_{\rm A}(t) = \sqrt{\frac{2\pi\hbar\omega_{\rm p}}{\mathcal{A}c}}[{\rm a}(t)e^{-i\omega_{\rm p}t} + {\rm a}^*(t)e^{i\omega_{\rm p}t}]. \qquad \text{(A1)}$$

Here ω_p is the laser carrier frequency, $\mathcal{A}$ is the cross-section of a laser wave, ${\rm a}(t)$ and ${\rm a}^*(t)$ are the complex am-

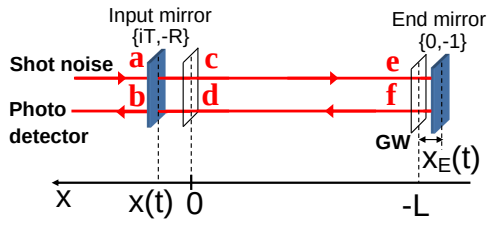

FIG. 14. Scheme of the simplest Fabry-Perot cavity

plitudes inside the cavity, considered in the signal range spectrum $\Omega \ll \omega_p$. The point in space of the considered field inside the cavity, where the light is considered, is determined by denoting the field amplitude with the corresponding letter (see notations in the FIG. 14) instead of $\mathrm{a}(t)$.

We consider two sources of light inside the cavity: (i) the light converted from carrier to sidebands by the differential mirror motion originates at the end-mirror with the amplitude $2E\frac{\omega_p}{c}x_E(t)$. (ii) The shot noise injection $\mathrm{a}(t)$ from the input mirror, corresponding to the SRM. The complex behavior of the light inside the cavity, according to the Maxwell equations, can be described, independently from its source, described, using the simple elements: propagation of light through the distance x introducing the additional phase shift $\omega_p\frac{x}{c}$, and the reflection from the mirrors with the transmission and the reflection coefficients, denoted as $\{iT, -R\}$.

We can effectively consider the field $\mathrm{c}(t)$ at the point of the tuned input mirror position as the result of the superposition of three different fields: (i) the input shot noise $\mathrm{a}(t)$ transmitted through the input mirror iT; (ii) the GW component injected half a round-trip ago $2E\frac{\omega_p}{c}x_E(t-\tau/2)$, and reflected from the input mirror $-R$, the microscopic displacement from the resonance position of which introduces the phase shift $e^{2i\omega_p\frac{x(t)}{c}}$; (iii) the field from the same point a round trip ago $\mathrm{a}(t-\tau)$, propagated towards the end-mirror, reflected back -1 (the phase shift due to GW end-mirror displacement is an effect of second order here), returned back to the input mirror and reflected from it $Re^{2i\omega_p\frac{x(t)}{c}}$:

$$\mathrm{c}(t) = iT_\mathrm{S}\mathrm{a}(t) + 2Re^{ik_\mathrm{p}x(t)}Ek_\mathrm{p}x_\mathrm{E}(t-\tau/2)+ \\ + Re^{2ik_\mathrm{p}x(t)}\mathrm{c}(t-\tau). \quad \text{(A2)}$$

Now we consider the fields from the shot noise and from the GW signal separately.

1. Impulse response to the GW end mirror motion

The fields from (A2) caused by only the gravitational wave read:

$$\mathrm{c}_\mathrm{gw}(t) = 2Re^{ik_\mathrm{p}x(t)}Ek_\mathrm{p}x_\mathrm{E}(t-\tau/2)+ \\ + Re^{2ik_\mathrm{p}x(t)}\mathrm{c}_\mathrm{gw}(t-\tau) \quad \text{(A3)}$$

and "gw" stands here for "gravitational waves".

From the solution, obtained by the recursive substitution of $\mathrm{c}_\mathrm{gw}(t)$ into the right part of the equation, the light reflected from the cavity $\mathrm{b}(t)$ reads

$$\mathrm{b}_\mathrm{gw}(t) = -2iTEk_\mathrm{p}x_\mathrm{E}(t-\tau/2)- \\ -\sum_{n=1}^{\infty} 2iTEk_\mathrm{p}R_\mathrm{S}^n \exp[\sum_{k=1}^{n} 2ik_\mathrm{p}x(t-k\tau)]x_\mathrm{E}(t-b\tau-\tau/2). \quad \text{(A4)}$$

The photocurrent after homodyne detection with the local oscillator (9) is

$$I_\mathrm{gw}(t) = \sum_{n=0}^{\infty} C_n^\mathrm{FP}\cos(\xi_n^\mathrm{FP}(t))x_\mathrm{E}\left(t-n\tau-\tau/2\right), \quad \text{(A5)}$$

where

$$C_0^\mathrm{FP} = -4\sqrt{2}\sqrt{\frac{\pi\hbar\omega_\mathrm{p}}{\mathcal{A}c}}T|E|k_\mathrm{p}, \quad \text{(A6a)}$$

$$C_n^\mathrm{FP} = C_0R^n, \quad \text{(A6b)}$$

$$\xi_0^\mathrm{FP}(t) = \phi_\mathrm{LO}, \quad \text{(A6c)}$$

$$\xi_n^\mathrm{FP}(t) = \phi_\mathrm{LO} + 2k_\mathrm{p}\sum_{k=1}^{n} x(t-k\tau). \quad \text{(A6d)}$$

The impulse response of the detector to the GW end-mirror motion is the photocurrent, caused by a delta-impulse GW signal:

$$L_{\mathrm{S}\to\mathrm{C}}(t,t_1) = \sum_{n=0}^{\infty} C_n^\mathrm{FP}\cos(\xi_n^\mathrm{FP}(t))\times \\ \times\,\delta\left(t-t_1+n\tau+\frac{\tau}{2}\right), \quad \text{(A7)}$$

2. The impulse response to the input shot noise

The quantum annihilation and creation operators of shot noise obey the equation (A2), since the Maxwell equations describes the evolution of quantum fields in the same way as of the classical fields. Using the same algebraic considerations, as in the previous subsection, for the solution of (A2) with the shot-noise only influence, one gets the field on the output:

$$\mathrm{b}_\mathrm{ip}(t) = \sum_{n=1}^{\infty} T^2\exp\left(i\varphi_n(t)\right)R^{n-1}e^{\omega_p(t_1-t)}\mathrm{a}(t-n\tau)- \\ - Re^{\omega_p(t_1-t)}\mathrm{a}(t)\exp i\varphi_0(t) + h.c., \quad \text{(A8)}$$

where the terms $\varphi_n(t)$ are equivalent to the ones in (28), and "ip" stands for "input port".

By setting a delta-like impulse on the field amplitude, we get the impulse response equivalent to $L^{\rm c}(t,t_1)$, defined in (24). The photo current of this field after the homodyne detection reads

$$I_{\rm ip}(t) = \int\limits_{-\infty}^{t} L^{\rm c}(t,t_1)\exp\left(i\omega_{\rm p}(t-t_1)\right) z(t_1)dt_1 + \\ + \text{h.c.} \quad \text{(A9)}$$

Here we introduce, equivalently to (26-28):

$$L_{\rm S}(t,t_1) = \sum_{n=1}^{\infty} T^2\exp\left(i\varphi_n(t)\right) R^{n-1}\delta(t_1-t+n\tau) - \\ - R\delta(t_1-t)\exp i\varphi_0(t), \quad \text{(A10)}$$

where

$$\varphi_0(t) = -2k_{\rm p}x(t), \quad \text{(A11a)}$$

$$\varphi_1(t) = 0, \quad \text{(A11b)}$$

and

$$\varphi_n(t) = 2k_{\rm p}\sum_{k=1}^{n-1} x(t-k\tau). \quad \text{(A11c)}$$

The autocorrelation function of the output noise may be obtained from the known input noise (22), using the impulse response (A9-A11):

$$B_\beta(t_1,t_2) = C_{\rm z}\delta(t_1-t_2). \quad \text{(A12)}$$

So, the output shot noise of the Fabry-Perot cavity with dynamically tuned SRM stays white independently from the end-mirror motion.

3. The equivalent Fabry-Perot cavity

The Fabry-Perot cavity, which is equivalent to the SRC, differs from the one, considered in the previous section of the appendix, by the non-ideal end-mirror with transmittance $T_{\rm F}$, equivalent to the optical losses in the cavity, and the corresponding reflectivity $R_{\rm F}$. This will modify the equations for the impulse response to the signal (A6) into

$$C_0^{\rm FP} = -4\sqrt{2}\sqrt{\frac{\pi\hbar\omega_{\rm p}}{\mathcal{A}c}}TR_{\rm F}|E|k_{\rm p}, \quad \text{(A13a)}$$

$$C_n^{\rm FP} = C_0(RR_F)^n, \quad \text{(A13b)}$$

$$\xi_0^{\rm FP}(t) = \phi_{\rm LO}, \quad \text{(A13c)}$$

$$\xi_n^{\rm FP}(t) = \phi_{\rm LO} + 2k_{\rm p}\sum_{k=1}^{n} x(t-k\tau). \quad \text{(A13d)}$$

The equation for the impulse on the input mirror shot noise injection (A10) would become:

$$L_{\rm S}(t,t_1) = \sum_{n=1}^{\infty} T^2\exp\left(i\varphi_n(t)\right) R^{n-1}R_{\rm F}^n\delta(t_1-t+n\tau) - \\ - R\delta(t_1-t)\exp i\varphi_0(t). \quad \text{(A14)}$$

The additional influence of the shot noise injected into the end mirror, equivalent to the noise from the optical losses reads:

$$L_{\rm S,em}(t,t_1) = T_{\rm F}T_{\rm S}e^{i\omega_{\rm p}\frac{\tau}{2}}\times \\ \times\sum_{n=0}^{\infty}\left(R_{\rm F}R\right)^n\exp[i(\Phi_N-\Phi_{N-n})]\times \\ \times\,\delta\left(t_1-t+\frac{\tau}{2}+n\tau\right), \quad \text{(A15)}$$

where "em" stands for "end-mirrors", and Φ_N is defined in (29a).

Appendix B: The impulse response of GEO 600

Considering the GEO 600 layout (FIG. 1) we may choose four sources of the light inside the SRC: (i) the signal input of the differential motion of the end mirrors

$$x_{\rm D}(t) = \frac{x_{\rm E}(t)-x_{\rm N}(t)}{2}, \quad \text{(B1)}$$

and the injections of shot noise (ii) into the dark port z(t) of GEO; two others (iii,iv) are the injections into the end mirrors u(t), r(t).

In contrast to appendix A we divide the light inside interferometer into the strong part with field amplitude A, A^*, belonging to the PRC, and the weak one $\mathrm{a}(t), \mathrm{a}^*(t)$, belonging to the SRC:

$$\hat{E}_A(t) = \sqrt{\frac{2\pi\hbar\omega_{\rm p}}{\mathcal{A}c}}(Ae^{-i\omega_{\rm p}t} + A^*e^{i\omega_{\rm p}t}) + \\ + \sqrt{\frac{2\pi\hbar\omega_{\rm p}}{\mathcal{A}c}}[\mathrm{a}(t)e^{-i\omega_{\rm p}t} + \mathrm{a}^*(t)e^{i\omega_{\rm p}t}]. \quad \text{(B2)}$$

All the other notations here are similar to ones in (A1).

1. Input-output relations

Here the input-output relations for the basic optical elements in the different arms are presented:

1. North arm (upwards from the beam splitter).

a. Common mode:

$$K = i\frac{\sqrt{2}}{2}H - \frac{\sqrt{2}}{2}E, \quad \text{(B3a)}$$

$$N = Ke^{ik_{\rm p}L_N}, \quad \text{(B3b)}$$

$$M = iA_NR - R_NN, \quad \text{(B3c)}$$

$$L = Me^{ik_{\rm p}L_N}. \quad \text{(B3d)}$$

b. Differential mode:

$$\mathrm{k}(t) = i\frac{\sqrt{2}}{2}\mathrm{h}(t) - \frac{\sqrt{2}}{2}\mathrm{e}(t), \tag{B4a}$$
$$\mathrm{n}(t) = \mathrm{k}(t - L_\mathrm{N}/c)e^{ik_\mathrm{p}L_\mathrm{N}}, \tag{B4b}$$
$$\mathrm{m}(t) = iA_\mathrm{N}\mathrm{r}(t) - R_\mathrm{N}\mathrm{n}(t) - 2iR_\mathrm{N}k_\mathrm{p}x_\mathrm{N}(t)N, \tag{B4c}$$
$$\mathrm{l}(t) = \mathrm{m}(t - L_\mathrm{N}/c)e^{ik_\mathrm{p}L_\mathrm{N}}. \tag{B4d}$$

2. East arm (right-hand side from the beam splitter).
a. Common mode:

$$J = i\frac{\sqrt{2}}{2}E - \frac{\sqrt{2}}{2}H, \tag{B5a}$$
$$S = Je^{ik_\mathrm{p}L_E}, \tag{B5b}$$
$$T = iA_\mathrm{E}U - R_\mathrm{E}S, \tag{B5c}$$
$$I = Te^{ik_\mathrm{p}L_\mathrm{E}}. \tag{B5d}$$

b. Differential mode:

$$\mathrm{j}(t) = i\frac{\sqrt{2}}{2}\mathrm{e}(t) - \frac{\sqrt{2}}{2}\mathrm{h}(t), \tag{B6a}$$
$$\mathrm{s}(t) = \mathrm{j}(t - L_\mathrm{E}/c)e^{ik_\mathrm{p}L_\mathrm{E}}, \tag{B6b}$$
$$\mathrm{t}(t) = iA_\mathrm{E}\mathrm{r}(t) - R_\mathrm{E}\mathrm{s}(t) - 2iR_\mathrm{E}k_\mathrm{p}x_\mathrm{E}(t)S, \tag{B6c}$$
$$\mathrm{i}(t) = \mathrm{t}(t - L_\mathrm{E}/c)e^{ik_\mathrm{p}L_\mathrm{E}}. \tag{B6d}$$

3. Signal recycling arm (downwards from the beam splitter).

Here we have the differential mode only:

$$\mathrm{g}(t) = i\frac{\sqrt{2}}{2}\mathrm{l}(t) - \frac{\sqrt{2}}{2}\mathrm{i}(t), \tag{B7a}$$
$$\mathrm{w}(t) = \mathrm{g}(t - L_S/c)e^{ik_\mathrm{p}L_\mathrm{S}(t)}, \tag{B7b}$$
$$\mathrm{o}(t) = iT_\mathrm{S}\mathrm{z}(t) - R_\mathrm{S}\mathrm{w}(t), \tag{B7c}$$
$$\mathrm{h}(t) = \mathrm{o}(t - L_\mathrm{S}/c)e^{ik_\mathrm{p}L_\mathrm{S}(t)}, \tag{B7d}$$
$$\mathrm{y}(t) = iT_\mathrm{S}\mathrm{w}(t) - R_\mathrm{S}\mathrm{z}(t). \tag{B7e}$$

$L_\mathrm{S}(t)$ here is the time-dependent distance from the SRM position to the beam splitter, setting the dynamical tuning. The change of this distance during the time of light travel between the beam splitter and the SRM is insignificant. L_N and L_E are the unperturbed lengths of the arms. The terms describing the information about GW in the field reflected from the north and the west arms are obtained from the fields of the power recycling mode by the linearization (like in e.g. [13]). The losses in the north end arms are reduced to the equivalent transmittances of the end mirrors, denoted by A_E and A_N.

2. Fields in the signal recycling cavity

Using equations (B4), (B6) and (B7), and the light trajectories from FIG.1, the field $\mathrm{h}(t)$ of the signal recycling mode can be effectively considered as the superposition of the following rays:

1. The shot noise field injected through the SRM $iT_\mathrm{S}z(t)$. Its phase is independent from the SRM position because it is transmitted by it. For convenience we assume the phase of $\mathrm{h}(t)$ to be in phase with $\mathrm{z}(t)$ by choosing an appropriate microscopic position of this point.

2. The field coming from the north mirror consists of the two parts: (i) the equivalent shot noise injection due to the optical losses in the arm $iA_\mathrm{N}r(t)$ and (ii) the signal part carrying the information about the north end-mirror position $-2iR_\mathrm{N}k_\mathrm{p}x_\mathrm{N}(t)N$. This field passes once through the north arm and the beamsplitter, followed by the reflection from the SRM with two corresponding passes through the signal recycling arm $e^{ik_\mathrm{p}(L_\mathrm{N}+2L_\mathrm{S})} \times \left(i\frac{\sqrt{2}}{2}\right) \times (-R_\mathrm{S})$, and its time delay is $L_\mathrm{N}/c + 2L_\mathrm{S}/c$.

2. The field coming from the east mirror consists of two parts: (i) the equivalent shot noise injection due to the optical losses in the arm $iA_\mathrm{E}u(t)$ and (ii) the signal part carrying the information about the east end-mirror position $-2iR_\mathrm{E}k_\mathrm{p}x_\mathrm{E}(t)E$. This field passes once through the east arm and the beamsplitter, followed by the reflection from the SRM with two corresponding passes through the signal recycling arm $e^{ik_\mathrm{p}(L_E+2L_S)} \times \left(-\frac{\sqrt{2}}{2}\right) \times (-R_\mathrm{S})$, and its time delay is $L_\mathrm{E}/c + 2L_\mathrm{S}/2$.

3. The field coming from the same point $\mathrm{h}(t-\tau)$ has two ways of propagation through the arms inside the SRC:

a. The part going through the north arm passes twice through the beam splitter, once reflected from each of the north and the SRM, and twice passes through each of the north and the signal recycling arms: $\left(i\frac{\sqrt{2}}{2}\right) \times \left(i\frac{\sqrt{2}}{2}\right) \times (-R_\mathrm{N}) \times (-R_\mathrm{S}) \times e^{2ik_\mathrm{p}(L_\mathrm{I}+L_\mathrm{S})}$. Its time delay is $2L_\mathrm{S}/c + 2L_\mathrm{N}/c$.

b. The part going through the east arm is reflected twice from the beam splitter, once reflected from each of the east and the SRM and passes twice through each of the east and the output arms: $\left(-\frac{\sqrt{2}}{2}\right) \times \left(-\frac{\sqrt{2}}{2}\right) \times (-R_\mathrm{E}) \times (-R_\mathrm{S}) \times e^{2ik_\mathrm{p}(L_\mathrm{S}+L_\mathrm{E})}$. Its time delay is $2L_\mathrm{S}/c + 2L_\mathrm{E}/c$.

The light has two clearly distinguishable time evolution processes: the microscopic change of the phase and the macroscopic time delay of the signal amplitude. The change of the phase, which is significant on the distance scales of the laser wavelength, determines the dark port condition:

$$e^{i2k_\mathrm{p}L_\mathrm{N}} = -e^{i2k_\mathrm{p}L_\mathrm{E}}, \tag{B8}$$

and the detuning of the SRM, which is taken into account in the expression $L_\mathrm{E} + L_\mathrm{S}(t) = L + x(t)$ as a microscopic displacement $x(t)$ from the length L of the equivalent cavity, resonant to the laser. The delays of the signal are caused mainly be the roundtrips with durations $\tau = 2L/c$, whilst the delays, introduced by the other distance scales in this model, can be neglected.

After the construction and simplification of the expression for the $\mathrm{h}(t)$ considered above, we get the following

expression for $\mathrm{o}(t)$:

$$\mathrm{o}(t) \approx 2R_\mathrm{S}R_\mathrm{F}Ek_\mathrm{p}x_\mathrm{D}(t-\tau/2)e^{ik_\mathrm{p}x(t)}+ + iT_\mathrm{S}\mathrm{z}(t)e^{-ik_\mathrm{p}x(t)} + i\frac{\sqrt{2}}{2}R_\mathrm{S}A_\mathrm{E}e^{ik_\mathrm{p}x(t)}\mathrm{v}(t-\tau/2)+ + i\frac{\sqrt{2}}{2}R_\mathrm{S}A_\mathrm{N}e^{ik_\mathrm{p}x(t)}\mathrm{r}(t-\tau/2)+ + R_\mathrm{S}R_\mathrm{F}e^{ik_\mathrm{p}[x(t)+x(t-\tau)]}\mathrm{o}(t-\tau). \quad \text{(B9)}$$

The terms in its right-hand side describe the contributions during one-round trip from different sources correspondingly: (i) from the signal end-mirror motion, (ii) from the shot noise injected into dark port, (iii) from the shot noise from the losses in the east mirror, (iv) from the shot noise from the losses in the north mirror. The fifth term of this formula describes the transformation of the field during a full round-trip in the SRC.

To get the impulse response to different signal sources we treat them separately.

3. The impulse response to the differential end mirror motion

The solution for the output field amplitude $\mathrm{y}(t)$ obtained from the corresponding part of (B9), using (B7) is the following:

$$\mathrm{y}_\mathrm{dm}(t) = -2iR_\mathrm{F}T_\mathrm{S}Ek_\mathrm{p}x_\mathrm{D}\left(t-\frac{\tau}{2}\right) - - 2i\sum_{n=1}^{\infty}R_\mathrm{F}^{n+1}R_\mathrm{S}^{n}T_\mathrm{S}Ek_\mathrm{p}x_\mathrm{D}\left(t-n\tau-\frac{\tau}{2}\right)\times \times\exp\left[2ik_\mathrm{p}\sum_{k=1}^{n}x(t-k\tau)\right], \quad \text{(B10)}$$

where "dm" stands here for "differential motion".

The photocurrent after the homodyne detection with the local oscillator $\sin(\omega_\mathrm{p}t+\phi_\mathrm{LO})$ of the field (B2) with this amplitude reads:

$$I_\mathrm{dm}(t) = \sum_{n=0}^{\infty}C_n\cos[\xi_n(t)]x_\mathrm{D}\left(t-n\tau+\frac{\tau}{2}\right), \quad \text{(B11)}$$

with C_n and $\xi_n(t)$ from (5). The impulse response (4) is obtained from here by setting a delta-impulse as the end mirror differential motion.

4. The impulse response to the injection into the dark port and into the end mirrors

The field caused by the injection of the shot noise into dark port is obtained considering the second term and the fifth term in (B10):

$$\mathrm{y}_\mathrm{dp}(t) = = \sum_{n=1}^{\infty}T_\mathrm{S}^2\exp\left[i\varphi_n(t)\right]R_\mathrm{F}^nR_\mathrm{S}^{n-1}e^{\omega_\mathrm{p}(t_1-t)}\mathrm{z}(t-n\tau)- - R_\mathrm{S}e^{\omega_\mathrm{p}(t_1-t)}\mathrm{r}(t)\exp\left[i\varphi_0(t)\right]+h.c., \quad \text{(B12)}$$

where "dp" stands for "dark port".

The corresponding photocurrent reads:

$$I_\mathrm{dp}(t) = \int_{-\infty}^{t}L^\mathrm{c}(t,t_1)\exp\left[i\omega_\mathrm{p}(t-t_1)\right]z(t_1)dt_1+ + h.c. \quad \text{(B13)}$$

The impulse response $L_\mathrm{S}(t,t_1)$ (27, 28), defined in (26), is obtained explicitly from (B12, B13).

The fields caused by the injection of the shot noise through the end mirror are

$$\mathrm{y}_\mathrm{nm} = A_NT_S\frac{\sqrt{2}}{2}\exp\left(i\omega_p\frac{\tau}{2}\right)\sum_{n=0}^{\infty}\left(R_FR_S\right)^n\times \times\exp[i(\Phi_N-\Phi_{N-n})]\mathrm{z}\left(t_1-t+\frac{\tau}{2}+n\tau\right) \quad \text{(B14a)}$$

and

$$\mathrm{y}_\mathrm{em} = A_ET_S\frac{\sqrt{2}}{2}\exp\left(i\omega_p\frac{\tau}{2}\right)\sum_{n=0}^{\infty}\left(R_FR_S\right)^n\times \times\exp[i(\Phi_N-\Phi_{N-n})]\mathrm{z}\left(t_1-t+\frac{\tau}{2}+n\tau\right), \quad \text{(B14b)}$$

where "nm" and "em" stand for "north mirror" and "east mirror" correspondingly. One gets (31) from this equation by substituting a delta-function input field.

5. Correspondence between the Fabry-Perot cavity and the GEO 600 models

The equivalence between the time-domain models of the Fabry-Perot cavity (FIG. 14) and of the GEO 600 layout (FIG. 1) may be established based on the comparison of the impulse responses, correspondingly (A6-A7) and (4-5), in the following characteristic cases:

(i) the end mirrors signal motion:

$$x_\mathrm{FP}(t) \equiv x_\mathrm{E}(t) = L_\mathrm{FP}\frac{h(t)}{2}, \quad \text{(B15)}$$

$$x_\mathrm{GEO}(t) \equiv \frac{x_\mathrm{E}(t)-x_\mathrm{N}(t)}{2} = L_\mathrm{GEO}\frac{h(t)}{2}; \quad \text{(B16)}$$

(ii) the injection into the cavity due to the signal motion:

$$\mathrm{e}_\mathrm{FP}(t) \equiv \mathrm{e}_\mathrm{GW}(t) = -2iE_\mathrm{FP}k_\mathrm{p}x_{FP}(t), \quad \text{(B17a)}$$

$$\mathrm{e_{GEO}}(t) \equiv \frac{\mathrm{t_{gw}}(t) - \mathrm{m_{gw}}(t)}{2} = \\ = -2iR_{\mathrm{F}}E_{\mathrm{GEO}}k_{\mathrm{p}}x_{\mathrm{GEO}}(t); \quad \text{(B17b)}$$

(iii) the evolution of the fields inside the cavity during single roundtrips:

$$\mathrm{e_{FP}}(t) = \mathrm{e_{FP}}(t-\tau)Re^{2ik_{\mathrm{p}}x(t-\tau/2)}, \quad \text{(B18a)}$$
$$\mathrm{e_{GEO}}(t) = \mathrm{e_{GEO}}(t-\tau)R_SR_Fe^{2ik_{\mathrm{p}}x(t-\tau/2)}; \quad \text{(B18b)}$$

(iv) the transmittance through the mirror towards the homodyne detector:

$$\mathrm{y_{FP}}(t) \equiv \mathrm{b_{GW}}(t) = iT\mathrm{e_{FP}}(t-\tau), \quad \text{(B19a)}$$
$$\mathrm{y_{GEO}}(t) \equiv \mathrm{y_{dm}}(t) = iT_{\mathrm{S}}\mathrm{e_{GEO}}(t-\tau). \quad \text{(B19b)}$$

From these relations we get the following parameters of the equivalent Fabry-Perot cavity:

$$L_{\mathrm{FP}} = L_{\mathrm{GEO}}, \quad \text{(B20a)}$$
$$E_{\mathrm{FP}} = R_{\mathrm{F}}E_{\mathrm{GEO}}, \quad \text{(B20b)}$$
$$R = R_{\mathrm{S}}R_{\mathrm{F}}, \quad \text{(B20c)}$$
$$T = T_{\mathrm{S}}. \quad \text{(B20d)}$$

Appendix C: Signal to noise ratio in the time domain consideration

The calculation of the SNR for the dynamically tuned detection of a chirp signal is based on the maximum likelihood principle, first described by Neyman and Pearson [29] and applied for the detection of known signals in the Gaussian noise, which is a good approximation after vetoing, e.g. in [30].

Assume the two hypotheses about the measured signal $x(t)$: (i) H_0, assuming a pure Gaussian noise $n(t)$ with the autocorrelation function $B(t,u)$, generally speaking non-stationary, without any signal, (ii) H_1, assuming the known signal $s(t)$ on the background of this noise:

$$x(t) = \begin{cases} n(t), 0 \geq t \geq T, \text{if } H_0 \text{ is true,} \\ s(t) + n(t), 0 \geq t \geq T, \text{if } H_1 \text{ is true.} \end{cases} \quad \text{(C1)}$$

For these hypotheses the probability distribution to measure the discrete number of signal values at the instances of time $x_i = x(t_i), 0 \geq i \geq N$ reads:

$$p_0(x_i) = \frac{1}{(2\pi)^{N/2}|S_{kl}|^{-1/2}} \times \\ \times \exp\left\{-\frac{1}{2}\sum_{i,j=0}^{N}[x_i - s(t_i)]S_{ij}^{-1}[x_j - s(t_j)]\right\}, \quad \text{(C2a)}$$

$$p_1(x_i) = \frac{1}{(2\pi)^{N/2}|S_{kl}|^{-1/2}} \exp\left\{-\frac{1}{2}\sum_{i,j=0}^{N}x_iS_{ij}^{-1}x_j\right\}, \quad \text{(C2b)}$$

where $S_{ij} \equiv E[(x_i - s(t_i))(x_j - s(t_j))]$ is the covariation matrix that describes the noise statistics.

The likelihood ratio for this signal is

$$\Lambda(x_i) \equiv \frac{p_1(x_i)}{p_0(x_i)} = \\ = \exp\left\{-\frac{1}{2}\sum_{i,j=0}^{N}[x_i - s(t_i)]S_{ij}^{-1}[x_j - s(t_j)] + \right. \\ \left. + \frac{1}{2}\sum_{i,j=0}^{N}x_iS_{ij}^{-1}x_j\right\}, \quad \text{(C3)}$$

The logarithm of likelihood for the continuous measurement may be obtained by the change of the sum over each index to the integration over the corresponding moment of time and the auxiliary substitution $q(t) = \int_0^T S^{-1}(t,t_1)s(t_1)dt_1$:

$$\log\Lambda[x(t)] = \int_0^T x(t)q(t)dt - \frac{1}{2}\int_0^T s(t)q(t)dt, \quad \text{(C4)}$$

where $q(t)$ is the solution of the following integral equation:

$$s(t) = \int_0^T q(u)B(t,u)du. \quad \text{(C5)}$$

The likelihood ratio $\Lambda[x(t)]$ depends on the measured data only through an integral called a detection statistics:

$$G = \int_0^T x(t)q(t)dt. \quad \text{(C6)}$$

According to assumptions, every measured value $x(t)$ is Gaussian, therefore G, being their linear combination, is also Gaussian, and the parameters of its distribution are $< G >= d^2$ (for H_1) and $\sigma_G =< G^2 - < G >^2 >= d^2$, where

$$d^2 = \int_0^T s(t)q(t)dt \quad \text{(C7)}$$

is the signal-to-noise ratio.

In a dynamic tuning detection task, $s(t)$ is the response of the photodector current to the GW from a CBC-coalescence and $B(t,u)$ is an autocorrelation function of noise. The integral equation (C5) in the case of white shot noise (33) reads:

$$s(t) = C_{\mathrm{z}}\int_0^T q(u)\delta(t-u)du = C_{\mathrm{z}}q(t), \quad \text{(C8)}$$

and its solution therefore

$$q(t) = \frac{s(t)}{C_{\rm z}}. \tag{C9}$$

The SNR, obtained from (C7), for the white shot noise is

$$d^2 = \frac{1}{C_{\rm z}} \int\limits_0^T s^2(t) dt. \tag{C10}$$

Appendix D: The algorithm of signal simulation

The expression for the output (4) consists of a very large number of summands, compared with the number of round trips during the signal detection, and therefore its numerical calculation inevitably requires the cut-off of this sum at some rather high number. We can use the following algorithm instead:

$$\begin{aligned} I_N &= \sum_{n=0}^{N-1} A_n x_{{\rm D}(N-n)} \cos(\phi_N - \phi_{N-n} + \phi_h) = \\ &= \sum_{n=0}^{M} A_n x_{{\rm D}(N-n)} \cos(\phi_N - \phi_{N-n} + \phi_h) + \\ &+ R^{M+1} \left[\cos(\phi_N - \phi_{N-M-1}) I_{N-M-1} - \right. \\ &\left. - \sin(\phi_N - \phi_{N-M-1}) I_{N-M-1({\rm sin})} \right], \end{aligned} \tag{D1}$$

where:

$$R = R_{\rm F} R_{\rm S}, \tag{D2a}$$

$$\begin{aligned} I_{N({\rm sin})} &= \sum_{n=0}^{N-1} A_n x_{{\rm D}(N-n)} \sin(\phi_N - \phi_{N-n} + \phi_h) = \\ &= \sum_{n=0}^{M} A_n x_{{\rm D}(N-n)} \sin(\phi_N - \phi_{N-n} + \phi_h) + \\ &+ R^{M+1} \left[\cos(\phi_N - \phi_{N-M-1}) I_{N-M-1({\rm sin})} \right. \\ &\left. + \sin(\phi_N - \phi_{N-M-1}) I_{N-M-1} \right] \end{aligned} \tag{D2b}$$

The whole information about the infinite decaying "tail" of the signal is used here to calculate the signal by including the phase shift, and the information about new "echoes".

The indices in (D1) are chosen in the following way:

$$\Delta\phi_k \equiv 2k_{\rm p} x((k-1)\tau) + \phi_{\rm F}. \tag{D3}$$

The whole chain of phase shift from the beginning of the measurement, cut after j round trips:

$$\phi_j \equiv \sum_{i=1}^{j-1} \Delta\phi_i. \tag{D4}$$

$$\phi_1 = 0. \tag{D5}$$

$$I_N \equiv I_{\rm y}((N-1)\tau), \tag{D6a}$$

$$x_{{\rm D}N} \equiv x_D((N-1)\tau - \tau/2). \tag{D6b}$$

The dynamical tuning resonance condition is

$$\phi_n - \phi_{n-1} = 2k_{\rm p} x_{n-1} = \frac{f_{n-1} + f_n}{2}\tau, \tag{D7}$$

where

$$f_{{\rm D}N} \equiv f((N-1)\tau - \tau/2) \tag{D8}$$

is an instantaneous chirp frequency.

[1] L. Santamaria, F. Ohme, P. Ajith, B. Brugmann, N. Dorband, M. Hannam, S. Husa, P. Mosta, D. Pollney, C. Reisswig, E. L. Robinson, and J. Seiler, Phys. Rev. D **82**, 064016 (2010).

[2] P. Ajith, Phys. Rev. D **84**, 084037 (2011).

[3] I. Kamaretsos, M. Hannam, S. Husa, and B. S. Sathyaprakash, Phys. Rev. D **85**, 024018 (2012).

[4] I. Kamaretsos, M. Hannam, and B. S. Sathyaprakash, Phys. Rev. Lett. **109**, 141102 (2012).

[5] T. Damour, A. Nagar, and L. Villain, Phys. Rev. D **85**, 123007 (2012).

[6] F. Pannarale, L. Rezzolla, F. Ohme, and J. S. Read, Phys. Rev. D **84**, 104017 (2011).

[7] B. F. Schutz, Nature **323** (1986).

[8] S. R. Taylor, J. R. Gair, and I. Mandel, Phys. Rev. D **85**, 023535 (2012).

[9] D. G. Blair, L. Ju, and C. Zhao, *Advanced Gravitational Wave Detectors* (Cambridge Univ PR, 2012).

[10] R. O'Shaughnessy, V. Kalogera, and K. Belczynski, Astrophys. J. **716** (2010).

[11] A. Buonanno and Y. Chen, Phys. Rev. D **67**, 062002 (2003).

[12] B. J. Meers, A. Krolak, and J. A. Lobo, Physical Review D **43** (1993).
[13] H. J. Kimble, Y. Levin, A. B. Matsko, K. S. Thorne, and S. P. Vyatchanin, Phys. Rev. D **65**, 022002 (2001).
[14] Y. Levin, Phys. Rev. D **57**, 659 (1998).
[15] Y. Levin, Phys. Lett. A **372**, 1941 (2008).
[16] G. M. Harry, A. M. Gretarsson, P. R. Saulson, S. E. Kittelberger, S. D. Penn, W. J. Startin, S. Rowan, M. M. Fejer, D. R. M. Crooks, G. Cagnoli, and N. Nakagawa, Class. Quatnum Grav. **19**, 897 (2002).
[17] Y. T. Liu and K. S. Thorne, Phys. Rev. D **62**, 122002 (2000).
[18] B. J. Offrein, H. J. W. M. Hoekstra, J. P. van Loenen, A. Driessen, and T. J. A. Popma, Optics Communications **112**, 253 (1994).
[19] M. J. Lawrence, B. Willke, M. E. Husman, E. K. Gustafson, and R. L. Byer, J. Opt. Soc. Am. B **16** (1999).
[20] M. Rakhmanov, *Dynamics of Laser Interferometric Gravitational Wave Detectors*, Ph.D. thesis, California Insitute of Technology Pasadena, California (2000).
[21] M. Rakhmanov, R. L. S. Jr., D. H. Reitze, and D. B. Tanner, Physical Letters A **305**, 239 (2002).
[22] http://www.geo600.uni hannover.de/geocurves/, "Geo 600 noise budget," (2006).
[23] H. Luck, "Private communication,".
[24] H. B. Callen and T. A. Welton, Phys. Rev. **83**, 34 (1951).
[25] K. Thorne, *in 300 Years of Gravitation* (Cambridge University Press, Cambridge, England, 1987) edited by S.W. Hawking and W. Israel.
[26] D. G. Blair, L. Ju, and C. Zhao, "Advanced gravitational wave detectors," (Cambridge Univ PR, 2012) Chap. 8, pp. 155–167.
[27] H. Grote, Class. Quantum Grav. **27** (2010).
[28] T. Fricke, N. Smith-Lefebvre, R. Abbott, R. Adhikari, K. Dooley, M. Evans, P. Fritschel, V. Frolov, K. Kawabe, J. Kissel, B. Slagmolen, and S. Waldman, Classical and Quantum Gravity **29**, 065005+ (2012), arXiv:1110.2815.
[29] J. Neyman and E. S. Pearson, Phil. Trans. R. Soc. A **231**, 289 (1933).
[30] B. J. Meers, A. Krolak, and J. A. Lobo, Physical Review D **48** (1993).